RESEARCH ARTICLE Open Access

Nonlinear nonlocal metasurfaces

Michele Cotrufo[1,2†], Luca Carletti[3,4†], Adam Overvig[1,5] and Andrea Alù[1,6*]

Abstract

Nonlinear metasurfaces have been enabling unprecedented control over light generation and wave mixing, demonstrating enhanced wavefront control, beam shaping and steering of nonlinear light waves. However, the design and operation of nonlinear metasurfaces have been for the most part limited to localized modes, fundamentally limiting the overall nonlinearity enhancement of such devices. Periodic structures supporting extended lattice resonances can realize much larger quality-factor resonances, and hence stronger nonlinearity enhancement, but they are fundamentally limited in their wavefront shaping capabilities, due to their high symmetry. Nonlocal metasurfaces have been recently introduced in linear settings to support highly delocalized resonant modes that can promote very large quality factors, yet without requiring periodicity, hence providing also local control over the wavefront. Here, we extend the powerful features of nonlocal metasurfaces to nonlinear phenomena, experimentally demonstrating nonlinear nonlocal metasurfaces that simultaneously support high quality factor modes, and hence strong nonlinearity enhancement, as well as a spatially varying geometric phase tailored over a subwavelength scale. We show how nonlinear nonlocal metasurfaces can at the same time enhance light-matter interactions, boosting nonlinear conversion efficiency, and enable precise subwavelength control over the wavefront of the generated light. Using this platform, we demonstrate a silicon metasurface for beam steering of third-harmonic generation in the visible. Our results show control over the polarization and steering angle of the third-harmonic signal, extending the framework of diffractive nonlocal metasurfaces to nonlinear optics, and pave the way for the development of nanoscale nonlinear devices with unparalleled control over the optical properties of generated light.

1 Introduction

Structuring matter at a subwavelength scale has enabled the creation of artificial materials with unprecedented optical properties and functionalities, surpassing natural materials. Over the past decades, intense research on optical nanoantennas and metasurfaces, based on metallic and/or dielectric nano-resonators, has led to breakthroughs in wavefront shaping [1–3], analog image processing [4, 5] and computing [6], imaging [7], optical holography [8], and information processing and encryption [9, 10]. This paradigm has been enabled by the deeply subwavelength control that metasurfaces can exert over key properties of light — such as polarization, directionality and frequency [11–15].

While these functionalities are all based on linear interactions of light with metasurfaces, these structured surfaces have also proven instrumental in controlling and enhancing nonlinear light-matter interactions, enabling efficient harmonic generation [16–19] and spontaneous parametric down-conversion [20, 21], relaxing phase matching constraints [17], and implementing optical limiting [22, 23], rectification [24] and nonreciprocal transmission [25, 26]. By tailoring optical nonlinearities

†Michele Cotrufo and Luca Carletti These authors contributed equally.

*Correspondence:
Andrea Alù
aalu@gc.cuny.edu
[1] Photonics Initiative, Advanced Science Research Center, City University of New York, New York, NY 10031, USA
[2] The Institute of Optics, University of Rochester, Rochester, NY 14627, USA
[3] Department of Information Engineering, University of Brescia, Via Branze 38, 25123 Brescia, Italy
[4] National Institute of Optics – National Research Council (INO-CNR), Via Branze 45, 25123 Brescia, Italy
[5] Department of Physics, Stevens Institute of Technology, Hoboken, NJ 07030, USA
[6] Physics Program, Graduate Center of the City University of New York, New York, NY 10016, USA

at subwavelength scales, two distinct fields of optics can be merged: nonlinear optics, which typically requires extended spatial scales, and nanoscale optics. As a result, nonlinear wavefront-shaping metasurfaces have emerged — ultrathin planarized devices that can generate higher harmonic frequencies while simultaneously imparting a locally tailored, spatially dependent engineered amplitude and phase on the generated wavefront. This feat, unique to nonlinear metasurfaces, has so far been achieved following two main paths, i.e., either by engineering localized resonances [27–29], or via an extension of the Pancharatnam–Berry phase to the harmonic generation process, also referred to as nonlinear geometric phase [30–34]. The latter enables a form of control over the amplitude and phase of the generated wavefront. These advantages are typically traded with some constraints on the polarization of the outgoing light and a limited field localization and enhancement, which in turn results in limited efficiency. Regardless of the approach, all demonstrations of nonlinear metasurfaces so far share a commonality: they rely on localized nanoscale resonances, which ensure a localized form of phase matching at the subwavelength scale and enable a subwavelength control over the nonlinear processes.

Recently, metasurfaces supporting nonlocal wave-matter interactions have been introduced, demonstrating remarkable features for several applications [3, 35]. Different from their local counterparts, nonlocal metasurfaces empower the coupling between their unit cell elements and leverage it to drastically enhance light-matter interactions, akin highly periodic grating-like structures supporting strong lattice resonances. However, different from conventional gratings, nonlocal metasurfaces also allow subwavelength local control over the amplitude, phase and polarization of the scattered wavefront [35, 36]. As such, nonlocal metasurfaces have been introducing a new paradigm for the spectro-spatial control of light [3], imaging [7] and analog computing applications [4, 5, 37]. So far, however, these demonstrations have been for the most part limited to the linear regime. Recently, nonlocal interactions in highly periodic grating-like structures supporting quasi bound states in the continuum (q-BICs) have proven advantageous for nonlinear light-matter interactions, both in terms of bandwidth selectivity and efficiency [38, 39]. While such periodic structures demonstrate enhanced light-matter interactions, they inherently showcase limited control over the nonlinear wavefront, both in terms of spatial shaping and polarization, due to their high symmetry. A key challenge remains: is it possible to tailor the local optical properties of a nonlinear metasurface that relies on nonlocal, lattice-supported phenomena? Such opportunity would combine the advantages of nonlocal metasurfaces in terms of high Q-factors, enhanced light-matter interactions, spectral selectivity and control, with the local wavefront shaping features conventionally associated with metasurfaces based on local resonances and lower Q-factors. These devices may expand the capabilities of multifunctional meta-optics to include active wavefront shaping by leveraging enhanced light–matter interactions enabled by high-Q resonances [40], broadband operation through stacking multiple metasurfaces supporting qBIC at slightly detuned wavelengths [3], and potential waveguide integration for photonic integrated circuits [41].

In this work, we address this challenge and demonstrate a nonlocal nonlinear metasurface supporting, simultaneously, a qBIC with high Q factor stemming from spatially extended nonlocal modes, and a spatially varying geometric phase tailored over subwavelength scales. We introduce rational design principles to tailor the nonlinear wavefront and experimentally demonstrate directional emission of third-harmonic generation (THG) at desired angles emerging from an ultrathin silicon metasurface. Our metasurface features directional emission modulation in response to different circular polarizations of the input pump. In past demonstrations of a nonlinear geometric phase in local metasurfaces, beam steering was shown for harmonic signals that are themselves circularly polarized, such that both the handedness and direction of the signal are affected by the handedness of the pump. In our nonlocal platform, the third harmonic (TH) emission is instead linearly polarized, irrespective of the pump handedness, while retaining the ability to steer its direction. This feature highlights the novel nature of the operating mechanism behind our metasurface, stemming from a two-step process depicted in Fig. 1: (1) a local resonant polarization couples the pump into a nonlocal mode with a customized geometric phase profile controlled by both the pump chirality and the metasurface geometrical phase (as described more quantitatively later); (2) the long-lifetime pump mode interacts with the silicon to efficiently generate a TH signal which inherits three times the phase gradient of the pump; the resulting engineered phase gradient results into scattering of the TH wave into a custom wave, and it can be leveraged to achieve steering towards preferential directions. In conjunction with the strong light-matter interactions inherent to delocalized qBICs, our demonstration highlights the potential of nonlocal metasurfaces to advance the boundaries of nonlinear nanophotonics.

2 Results

We begin our analysis by considering a metasurface design formed by a periodic repetition of the unit-cell shown Fig. 2a. The unit cell consists of two rectangular apertures, rotated by 90° with respect to each other,

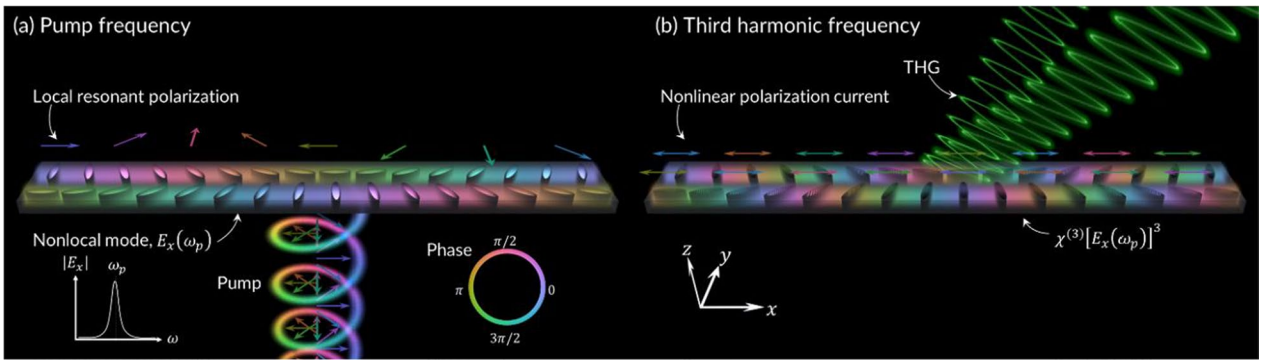

Fig. 1 Working principle of the proposed nonlinear nonlocal metasurface. (**a**) A nonlocal metasurface is excited from below by circularly polarized light at the pump frequency, ω_p. The metasurface has a locally tailored resonant polarization, depicted by the colored arrows above the metasurface. The colors of the array track the phase of the coupling process, inherited from the polarization-dependent phase of the incident circular polarization. As a result, a nonlocal mode, characterized by the field component E_x, is excited within the metasurface with a resonantly enhanced amplitude and a spatial gradient of phase along the *x* direction. (**b**) The third-harmonic generation process in the metasurface is characterized by the quantity $\chi^{(3)}\left[E_x(\omega_p)\right]^3$, which inherits three times the phase gradient from the pump. The resulting nonlinear polarization currents, denoted by colored arrows, scatter the third harmonic to the far field in a direction dictated by the engineered phase gradient, with two diffraction orders in the y direction due to the superwavelength periodicity of the metasurface

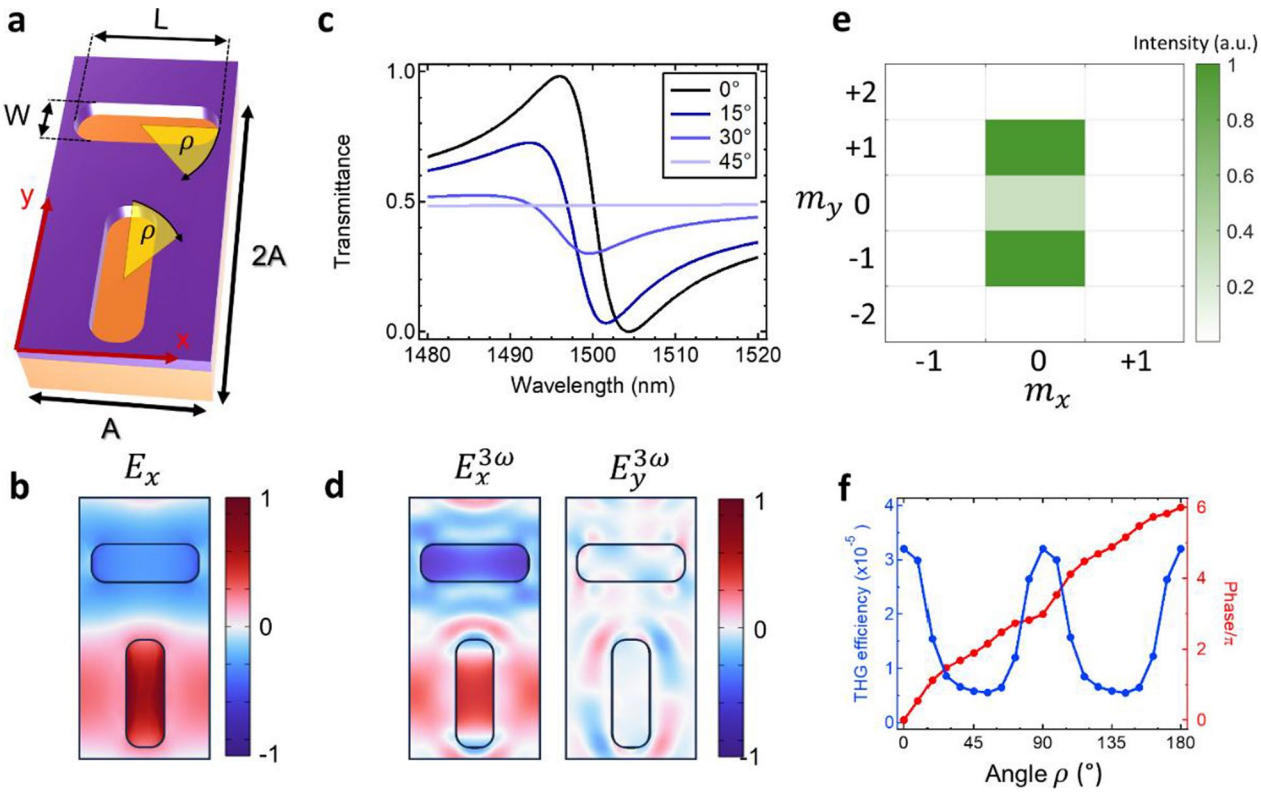

Fig. 2 Metasurface unit-cell and numerical investigation. (**a**) Schematic representation of the unit-cell. (**b**) Profile of the *x*-component of the electric field in the horizontal plane of the metasurface at the qBIC wavelength (1500 nm). (**c**) *x*-polarized transmittance spectrum of a periodic metasurface with unit cell shown in panel (a), as ρ changes from 0° to 45°. (**d**) Electric field distribution (*x* and *y* components) in the horizontal plane of the metasurface at the TH wavelength when the pump is at a wavelength of 1500 nm. (**e**) Distribution of the TH emission into different far-field diffraction orders (m_x, m_y). (**f**) THG conversion efficiency and phase of the TH signal in the (0,1) diffraction order as a function of ρ

and etched into a thin film of amorphous silicon (a-Si) placed on a silica substrate. The unit-cell is rectangular with periods A and $2A$ along the x and y directions, respectively. The geometric phase is encoded by rotating each aperture around its center by an angle ρ, as defined in Fig. 2a. We first consider periodic metasurfaces, i.e., arrays obtained by a periodic repetition of the unit-cell shown in Fig. 2a and with fixed value of the angle ρ . The metasurface design is obtained through numerical analysis in COMSOL (see Methods for details on the numerical calculation technique). Based on an eigenmode study, we optimized the geometrical parameters such that the metasurface supports a qBIC at the wavelength of 1500 nm. The optimized design consists of an a-Si film with thickness of 125 nm, period $A=445$ nm and aperture width $L=371$ nm. By varying the aspect ratio δ, defined as $\delta=(L-W)/L$ (where W is the short length of the apertures), we can control the Q-factor of the resonance. We used $\delta=0.66$, yielding a Q-factor of 180, which allowed us to obtain a resonant bandwidth large enough to accommodate the full bandwidth of the laser used later for the nonlinear characterization (see Methods for details on the experimental setups). Figure 2b shows the x-axis component of the electric field in the xy-plane in the middle of the a-Si film, under x-polarized normal-incidence resonant excitation and for $\rho = 0°$. The response shows an antisymmetric phase profile, typical for symmetry-protected qBICs.

We used finite-element-method calculations implemented in COMSOL to numerically estimate the transmittance spectra of periodic metasurfaces for different values of ρ and fixed x-polarized excitation (Fig. 2c). For $\rho = 0°$, the spectrum features the characteristic Fano lineshape associated to a qBIC. By varying the angle ρ, we control the coupling efficiency between the qBIC and free-space wave for a given polarization [32], while having a minimal effect on the qBIC wavelength. Indeed, as confirmed by Fig. 2c, as the angle ρ changes from 0° to 45° the x-polarized transmittance spectrum evolves from a high-contrast Fano lineshape ($\rho = 0°$) to a flat line ($\rho = 45°$). The absence of any spectral feature for $\rho = 45°$ confirms that, for this value of ρ, the qBIC does not couple to x-polarized light. The opposite trend with respect to ρ is observed for a y-polarized excitation (see Section S2 in the Supplemental Information). Thus, by using circularly polarized light, which contains both x and y polarized electric fields, the qBIC can be excited for any rotation angle ρ (see Section S2 in the Supplemental Information). These effects are robust with respect to small variations of the rod dimensions due to fabrication imperfections (see Section S5 in the Supplemental Information). While the induced electric field amplitude is nearly uniform as a function of ρ, and the resulting transmission amplitude is constant, by varying ρ we control the phase of the metasurface response through a geometric phase. In contrast to the conventional geometric phase approach used in local metasurfaces, which yields a $\Phi_{geo} \approx 2\rho$ phase factor, here the geometric phase has the approximate form $\Phi_{geo} \approx 4\rho$. The additional factor of two arises from the two-step process of the underlying resonant scattering phenomenon: coupling into the qBIC yields one factor 2ρ, while coupling out yields an additional factor 2ρ. As a result, the near field profile of the qBIC is patterned with a 2ρ dependence, and the outcoupled light is patterned with 4ρ. [32]

To characterize the geometric phase encoded by the structure on the THG wavefront, we analyze the effect of the rotation angle ρ on the phase and amplitude of the TH signal emitted by a periodic metasurface with unit-cell shown in Fig. 2a. We performed numerical simulations of the THG process in COMSOL based on the induced nonlinear polarization in the a-Si film. Due to the material isotropy, intrinsic permutation symmetry implies that the elements of the third-order nonlinear susceptibility tensor, $\hat{\chi}^{(3)}$, for THG are given by $\chi^{(3)}_{ijkl} = \chi^{(3)}(\delta_{ij}\delta_{kl} + \delta_{ik}\delta_{jl} + \delta_{il}\delta_{jk})$. This results in a nonlinear polarization for the THG, $\overline{P}(3\omega)$, that can be expressed as [31, 32]

$$\overline{P}(3\omega) = \varepsilon_0 \hat{\chi}^{(3)} \vdots \overline{E}\overline{E}\overline{E} = 3\varepsilon_0 \chi^{(3)} (\overline{E} \cdot \overline{E})\overline{E} \quad (1)$$

where $\overline{E} \cdot \overline{E} = E_x^{\,2} + E_y^{\,2} + E_z^{\,2}$, $\overline{E}$ is the electric field vector at the pump frequency, $\chi^{(3)}$ is the nonlinear susceptibility of amorphous silicon, and ε_0 is the vacuum permittivity. As shown in Fig. 2b and further discussed in Section S3 of the Supplemental Information, for $\rho = 0°$ the electric field of the qBIC is predominantly polarized along the x-axis. This, together with the material isotropy, ensures that the THG nonlinear polarization (Eq. 1) retains the same polarization. In addition, we expect the TH to be emitted mainly into the $(m_x, m_y) = (0, \pm 1)$ diffraction orders because (i) the electric field phase is odd-symmetric with respect to the x-axis (see Fig. 2b), and (ii) the unit-cell is subwavelength along the x-axis but superwavelength along the y-axis. This is confirmed by the calculated electric field distribution in the middle plane of the metasurface (Fig. 2d), and by the calculated far-field TH emission into the different diffraction orders (Fig. 2e).

When the angle ρ is different than zero, the near field induced by a circularly polarized pump acquires an additional geometric phase factor equal to $\pm 2\rho$ (where the $\pm$ sign depends on the pump chirality), stemming from the coupling process described above [3]. Thus, the electric field at the pump frequency inside the metasurface can be expressed as $Ee^{\pm i2\rho}$ where the $e^{\pm i2\rho}$ term represents the acquired phase difference. This phase is then

imprinted onto the phase of the TH polarization $P_i(3\omega)$: since the latter is proportional to the cube of the pump electric field, it will in general be proportional to a term $E_\alpha E_\beta E_\gamma e^{\pm i2\rho} e^{\pm i2\rho} e^{\pm i2\rho}$ where α, β, γ are equal to R or L, for right- or left-circularly polarized light, and the sign of the exponent is accordingly chosen. If we assume, for example, that the pump is left-handed circularly polarized, and neglecting conversion between opposite circular polarizations in the structure, the nonlinear polarization reads

$$P_{x,\rho}(3\omega) = \varepsilon_0 \chi^{(3)} \left(E_R^3 e^{-i6\rho} + E_L^3 e^{i6\rho} + E_L E_R^2 e^{-i2\rho} + E_R E_L^2 e^{i2\rho} \right) \approx \varepsilon_0 \chi^{(3)} \, \mathrm{E}_\mathrm{L}^3 e^{i6\rho} \tag{2}$$

where E_R and E_L denote the right- and left-handed circularly polarized components of the pump electric field. The TH phase and geometrical angle ρ relation predicted by Eq. (2) are numerically verified in Fig. 2f. As shown by the red solid line in Fig. 2f, as ρ changes, the phase of the co-polarized TH signal is approximately equal to 6ρ. Moreover, the TH efficiency (solid blue line in Fig. 2f), defined as the ratio between TH and pump powers, oscillates as ρ varies. This is due to a small spectral shift of the qBIC wavelength as ρ changes (see also Figure S3 in the Supplemental Information) and to the fact that, in simulations, we assume a monochromatic excitation. In the experiments, this small spectral shift is mitigated by the fact that the laser linewidth is comparable to the qBIC wavelength. These effects could be further mitigated by also varying the lengths L and W (as ρ varies) to keep the qBIC wavelength constant.

Thus, while a rotation of the apertures by an angle ρ can largely affect the coupling to free-space radiation with a fixed linear polarization, the qBIC wavelength is only slightly perturbed. Local control of the phase of the THG can hence be achieved at the sub-wavelength scale, even though the pump relies on a nonlocal mode to efficiently excite the nonlinearity. As such, Fig. 2f can be used as a rational library or lookup table to design wavefront shaping nonlocal nonlinear metasurfaces which impart spatially varying phase profiles on the generated TH signal.

To demonstrate this phenomenon for nonlinear wavefront shaping, we designed and fabricated a phase-gradient metasurface for beam-steering and boosting the TH emission close to the wavelength of 500 nm. The phase-gradient metasurface is obtained by defining a super-cell composed of 16 unit-cells disposed along the x-axis, with ρ gradually varying from 0° to 180°, as sketched in Fig. 1. Based on the previous derivation, we expect the phase of the TH beam to vary by 6π radians along the super-cell, resulting in a steering angle of about 12°. Figure 3a shows a top-view SEM picture of the fabricated device, with insets showing zoomed-in views of the super-cell (dashed blue box) and unit-cell (dashed red box). The measured transmittance spectrum upon x-polarized illumination (Fig. 3b, solid blue line) shows a pronounced Fano lineshape with a dip close to 1530 nm. This resonance feature is very similar to the numerically calculated spectrum for a periodic array (Fig. 2c), indicating that our local perturbation of the periodic geometry, aimed at preserving the spatially extended resonance, does not critically degrade the qBIC features.

In order to verify the role of this resonance in boosting the TH emission, we performed a preliminary experiment (Fig. 3b and c) where the metasurface is excited from the glass side with an H-polarized pump laser at the FF wavelength (we label with H the linear polarization parallel to the x-axis, see reference frame in Fig. 3a), and the TH signal is collected in transmission with a low-NA lens (NA = 0.25, focal length 5 cm). In these and the following measurements, the excitation spot was kept large (diameter of the order of 140 μm) to properly couple to the spatially delocalized nonlocal resonance. The excitation was provided by a pulsed laser (repetition rate of 80 MHz, pulse duration of 2 ps) with a central wavelength λ_{FF} that can be tuned across the spectral band of the qBIC. The red-shaded area in Fig. 3b shows a representative spectrum of the pump laser. The collected TH emission was directed either to a spectrometer, or to a calibrated photodiode, which allows us to measure the absolute TH power and thus the THG efficiency. In Fig. 3c we show the average power of the TH emission (P_{THG}) as a function of pump average power P_{FF} for $\lambda_{FF} = 1527$ nm. The TH power features the expected trend $P_{THG} = \eta P_{FF}^N$ with $N = 3.36$ and $\eta = 2 \cdot 10^{-6} W^{-2}$, where the value of the exponent N confirms the third-order nature of the observed frequency conversion. The discrepancy between the observed power law and a perfect cubic dependence (N = 3) is likely due to the occurrence of additional nonlinearities, such as self-induced thermo-optic effects, which shift the resonant wavelength of the qBIC and thus alter the cubic power-law expected for the THG power. In particular, recent experiments [25] performed in similar experimental conditions have demonstrated the occurrence of large thermo-optic effects in amorphous silicon metasurfaces with Q factors similar to the ones employed here, leading to wavelength shifts comparable to the resonance linewidths. At the highest pump power considered in our experiment ($P_{FF} \approx 0.26$ W), the conversion efficiency P_{THG}/P_{FF} was

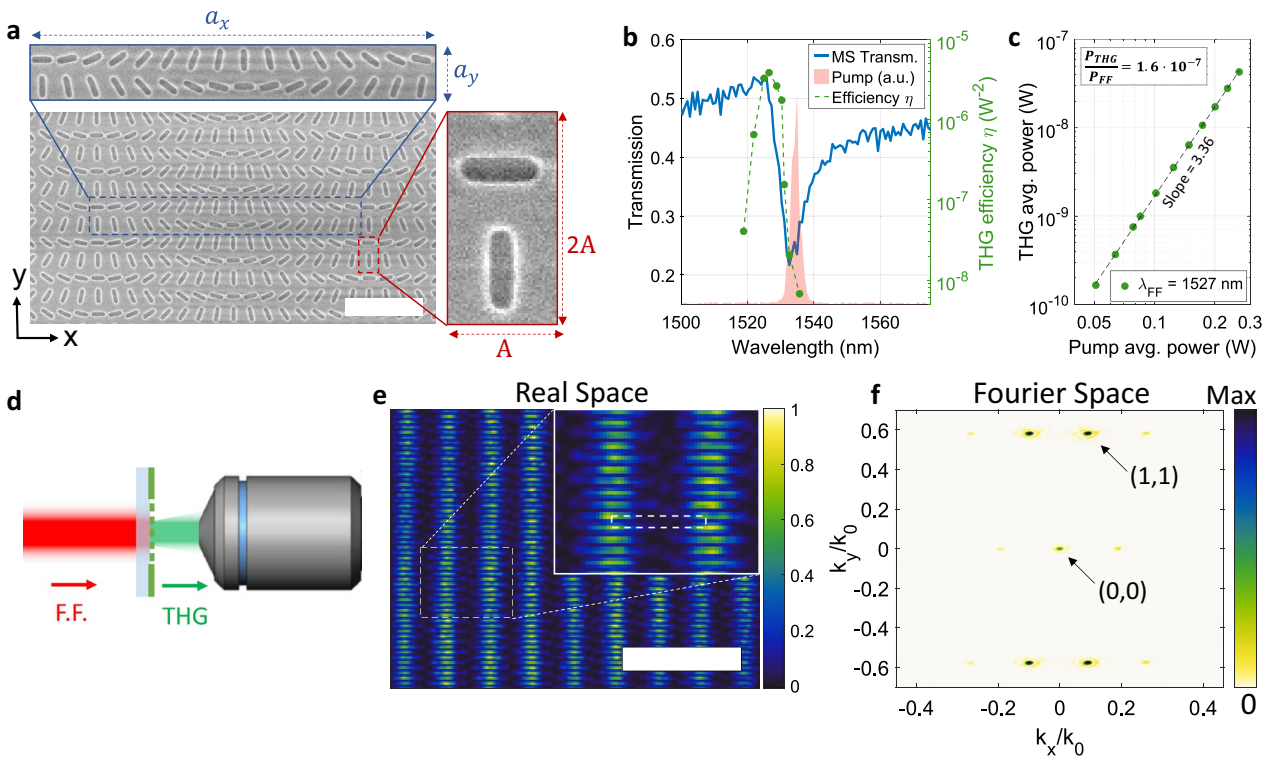

Fig. 3 Device fabrication, experimental setup and characterization. (**a**) SEM micrograph of the fabricated silicon nonlocal metasurface, scalebar = 2 μm. The two insets show zoomed-in views of the super unit-cell (blue-edged rectangle) with dimensions a_x = 7.12 μm and a_y = 0.89 μm, and of the unit-cell (red-edged rectangle) with dimensions A = 0.445 μm and 2A. (**b**) Left vertical axis: normal-incidence *x*-polarized transmission spectrum (blue solid line), and a typical spectrum of the pump laser (red shaded spectrum, intensity in arbitrary units). Right vertical axis: THG efficiency η (as defined in the text) versus central wavelength of pump laser (green circles). (**c**) THG average power versus pump average power, for the pump wavelength at which the highest efficiency in panel b is obtained (1527 nm). (d) Schematic of the experimental configuration (see Methods for additional information). (**e**) Real-space imaging of the TH emission under H-polarized pump. Scalebar = 20 μm. Inset: Zoomed-in view of the real-space TH emission, corresponding to the dashed white rectangle in panel (e). The dashed white rectangle in the inset denotes the size of the super unit-cell. (**f**) Measured k-space imaging of the TH emission, showing the TH intensity as a function of the normalized in-plane wavevector components k_x/k_0 and k_y/k_0, for an *x*-polarized pump. Note that the colorscale of this colorplot has been intentionally saturated to better show the position of the other diffraction orders with weaker intensity

on the order of $1.6 \cdot 10^{-7}$. However, as explained later, this value largely underestimates the actual metasurface THG efficiency, since most of the TH power is emitted at larger angles, not captured by the low-NA lens used in the measurements in Fig. 3(b-c). We repeated this measurement varying the pump central wavelength λ_{FF} across the Fano lineshape and measured the corresponding wavelength-dependent efficiency $\eta(\lambda_{FF})$, which is plotted as green circles in Fig. 3b. This data confirms the resonant enhancement provided by the metasurface: the efficiency $\eta(\lambda_{FF})$ peaks at $\lambda_{FF} = 1527$ nm and it remains relatively constant in the [1525nm, 1530nm] wavelength range, while it drops by more than one order of magnitude for detuned wavelengths.

After this initial characterization, we experimentally investigated angle- and polarization-dependence of the TH emission, and its correlation to the pump polarization, using a large-NA objective (40x, NA = 0.95) for the THG collection. Figure 3e shows real-space imaging of the TH emission for an H-polarized pump, confirming that the TH emission is delocalized in real space, and its spatial pattern follows the metasurface periodicity. By imaging the back-focal-plane (BFP) of the objective onto the camera (see Methods for additional details), we measured the polarization-resolved angle-dependent TH emission, quantifying the intensity and polarization of each TH diffraction order. Figure 3f shows a subset of the measured data, reporting the TH intensity versus the in-plane wavevector components k_x and k_y for the case in which the pump is H-polarized and the H component of the TH emission is selected. The *k*-space TH emission shows four main bright spots, with approximately the same intensities, corresponding to the four diffraction orders $(m_x, m_y) = (\pm 1, \pm 1)$. This result is intuitively

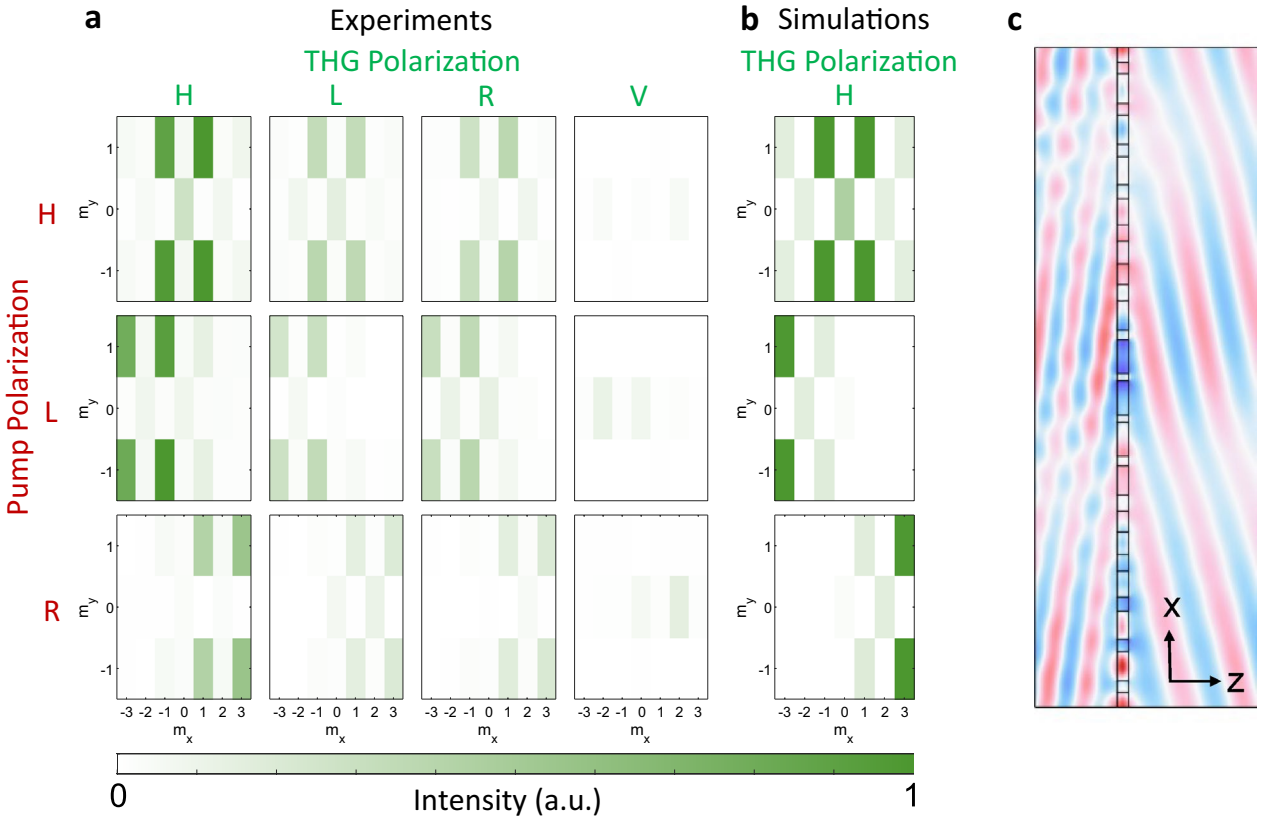

Fig. 4 k-space emission of the TH signal versus pump and TH polarization. (**a**) Histograms showing experimentally measured k-space TH emission into different diffraction orders, labelled by the integers m_x and m_y, for different combinations of pump and TH polarization. In each plot, the pump polarization is shown on the left of the corresponding row, while the measured TH polarization component is shown at the top of corresponding column. H = horizontal, V = vertical, L = left circularly polarized, R = right circularly polarized. The corresponding raw data are shown in the Supplementary Information. All histograms share the same colorscale. (**b**) Same data as in panel (**a**) but obtained from numerical calculations, and for a fixed TH polarization equal to H. (**c**) Numerical calculation of the H-polarized electric field of the TH signal generated by the metasurface in the xz-plane. The emitted wavefront shows the steering of the TH signal

expected based on our analysis in Fig. 2: when using an H-polarized pump, only the two unit-cells with $\rho = 0°$ and 180° efficiently couple to the qBIC [see Fig. 2c]. Thus, a 2π rad phase shift is accumulated in the super-cell, corresponding to an emission angle of about 4°, or the $(\pm 1, \pm 1)$ diffraction orders of the phase-gradient metasurface.

To demonstrate that our phase-gradient metasurface can perform THG beam steering controlled by the chirality of the pump, we repeated the measurement in Fig. 3f for different combinations of pump and TH polarization components. Our results verify the theoretical prediction that (i) when the pump is circularly polarized, the TH is preferentially emitted towards either the $x > 0$ or $x < 0$ semi-spaces depending on the pump chirality, and that (ii) the polarization of the TH remains always horizontal (H), regardless of the pump polarization. The raw measurement data are shown in the Supplementary Information, while Fig. 4a reports the experimental results collected in histograms. For each measurement, the pump polarization is reported on the left of the corresponding row, while the measured TH polarization component is shown at the top of corresponding column ('H' = horizontal, 'V' = vertical, 'L' = left circularly polarized, 'R' = right circularly polarized). In each histogram, each bin corresponds to the intensity emitted towards a particular diffraction order (m_x, m_y), as denoted in each plot axis, and it is obtained by integrating the corresponding intensity map within the relevant k-space region. To aid quantitative comparison, all histograms in Fig. 4a share the same colorscale (reported at the bottom).

We first focus on the case in which the pump is H-polarized, corresponding to the four histograms in the top row of Fig. 4a. The experimentally measured histograms confirm that, when the pump is H-polarized, the k-space emission pattern is dominated by the $(\pm 1, \pm 1)$ diffraction orders, and that the TH emission features a clear left–right spatial symmetry: the TH emission

towards the semi-space $x > 0$ is perfectly mirrored by the TH emission towards the semi-space $x < 0$. This is expected because, as explained above, for H-polarized pump only two unit-cells couple efficiently to free-space radiation, and no geometric phase is accumulated. Thus, under H-polarized pump there is no preferential direction of TH emission. Moreover, the top-right plot in Fig. 4a (H-polarized pump, V-polarized TH signal) shows that the vertically polarized component of any TH diffraction order with $m_y \neq 0$ is zero. Thus, as expected in our theoretical model, the TH emission associated with these orders is H-polarized for any pump polarization, inheriting the primary polarization of the qBIC near field (as shown in Fig. 2b and 2d), which is independent of the polarization used to excite it.

Next, we focus on the case in which the pump polarization is modified from linear to circular (shown in the middle and bottom rows of Fig. 4a). The measurements show that symmetry breaking occurs in the k-space emission pattern. In particular, for the L-polarized pump (middle row of Fig. 4a), the intensity of all diffraction orders with $m_x < 0$ becomes much higher than the intensity of all diffraction orders with $m_x > 0$. In fact, the latter completely disappear from the k-space pattern. Moreover, for any TH polarization except the vertical one, the diffraction orders $(-3, \pm 1)$ are much brighter, and their intensity is comparable to the one of the diffraction orders $(-1, \pm 1)$. When the pump chirality is switched from left (middle row of Fig. 4a) to right (bottom row of Fig. 4a) the opposite effect is observed.

To summarize, the experimental measurements in Fig. 4a confirm that the TH emission direction is efficiently controlled by the pump chirality. This is expected from our model and Eqs.1, 2, since inverting the chirality of the pump changes the sign of the nonlinear geometric phase. In Fig. 4b, we show numerical calculations of the angle-resolved TH emission for different pump polarizations and for a fixed H polarization of the TH emission. We observe an excellent agreement between these calculations and the corresponding experimental data (left-most column of Fig. 4a), albeit with slightly different ratios between the intensities of the different diffraction orders, which can be attributed to small fabrication and experimental nonidealities. In Fig. 4c we show the calculated H-polarized electric field component of the TH generated by a L-polarized pump, in the xz-plane of the metasurface, confirming the expected steering of TH emission. Furthermore, the measurements in Fig. 4a confirm that the $(\pm 3, \pm 1)$ diffraction orders of the TH emission are always H-polarized, for any pump polarization (i.e., for any row in Fig. 4a). This demonstrates that the TH polarization is independent of the pump polarization, and that the TH emission does not carry any preferential chirality, even when the pump is circularly polarized. This is due to the combination of the dominant x-axis component of the electric field of the qBIC (see Fig. 2b) and the isotropic nature of the $\chi^{(3)}$ tensor of a-Si. To quantitatively confirm the polarization properties of the TH emission, we used the data in Fig. 4a to calculate the polarization content and the degree of linear polarization of the diffraction orders with the highest intensity for all possible pump polarizations. We found that, for all these orders, the H-polarized component of the TH is above 92% of the total intensity, and that the degree of linear polarization is above 96%. We also note that the experimental measurements in Fig. 4a feature some asymmetry between the intensities of the dominant diffraction orders for the cases in which the pump is L-Polarized (Fig. 4a, mid row) or R-Polarized (Fig. 4a, bottom row). Such asymmetries, not expected from simulations (Fig. 4b), are attributed to imperfections in the fabrication process which might result in small random fluctuations and/or systematic drifts in the lengths and widths of the 32 rods which form each super unit cell. Indeed, since the intensity emitted into each diffraction order is due to a coherent sum of the TH generated from each point of the super unit cell, it is expected that small fluctuations of the rod geometry might lead to non-negligible asymmetries of the diffracted intensity.

Importantly, the BFP measurements shown in Fig. 4 also allow us to provide a better estimation of the TH efficiency measured in Fig. 3b-c. In the measurements in Fig. 3b-c, because of the low (NA = 0.25) of the collection lens used, only the diffraction orders (0,0) and (±1,0) contributed to the measured THG power. However, the measurements in Fig. 4 reveal that about 93% of the TH is actually emitted in the $(\pm 1, \pm 1)$ and $(\pm 3, \pm 1)$ diffraction orders. Taking this into account to correct the values reported in in Fig. 3b-c, we estimate a maximum THG efficiency (for average powers) of $\eta \approx 3.3 \cdot 10^{-5} W^{-2}$. In terms of peak powers, the efficiency is $\eta \approx 8.5 \cdot 10^{-13} W^{-2}$, which is almost two orders of magnitudes larger than previously reported nonlinear gradient metasurfaces [32, 34], and several orders of magnitude larger than what obtained with different types of local metasurfaces (See Section S4 in the Supplemental Information for a detailed comparison between our work and previous ones). The total power conversion efficiency is estimated $P_{\mathrm{THG}}/P_{\mathrm{FF}} \approx 2.3 \cdot 10^{-6}$ at $\lambda_{\mathrm{FF}} = 1527$ nm and $P_{\mathrm{FF}} = 0.25 W$. This enhancement of conversion efficiency stems from the use of qBIC at the pump rather than localized Mie-type resonances.

Finally, we systematically investigated how the intensity of each diffraction order of TH emission depends on the pump ellipticity (Fig. 5). To this end, we fixed the TH detection polarization to H, and we recorded the

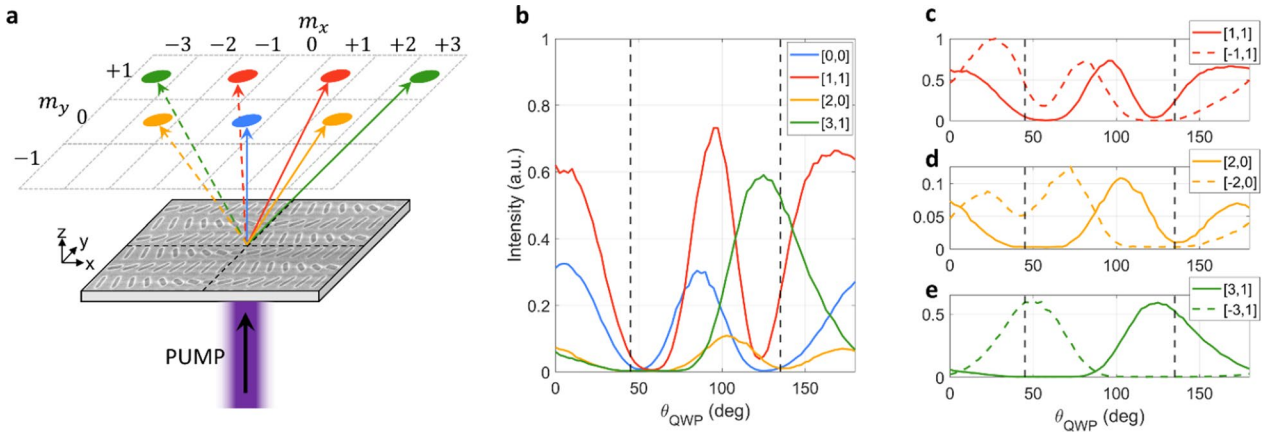

Fig. 5 Intensity of different diffraction orders versus ellipticity of pump polarization. The pump was polarized with a linear polarizer set to horizontal followed by a quarter-wave plate with variable angle θ_{QWP} of the fast axis. The values $\theta_{QWP} = 0°, 90°, 180°$ correspond to horizontally polarized pump, while $\theta_{QWP} = 45°$ and $\theta_{QWP} = 135°$ correspond to circularly polarized pump with left and right chirality, respectively. (**a**) Each diffraction order shown in panels (b)-(e) is color-coded according to the colored circles shown in this panel. (**b**) Intensity of the diffraction orders (0,0), (1,1), (2,0), (3,1) versus θ_{QWP}. (**c**) Intensity of the diffraction orders (±1,1) versus θ_{QWP}. (**d**) Intensity of the diffraction orders (±2,0) versus θ_{QWP}. (**e**) Intensity of the diffraction orders (±3,1) versus θ_{QWP}. The vertical dashed lines in panels (**b**)–(**e**) correspond to the cases in which the pump has a circular polarization

k-space TH emission while continuously varying the ellipticity of the pump polarization by rotating a quarter wave plate placed in the pump path (after a linear polarizer). In Fig. 5b-e, θ_{QWP} denotes the position of the fast axis of the quarter wave plate, defined such that the values $\theta_{QWP} = 0°, 90°, 180°$ correspond to an H-polarized pump, while $\theta_{QWP} = 45°$ and $\theta_{QWP} = 135°$ correspond to L and R-polarized pump, respectively. In Fig. 5b–e, we show the measured intensity of different diffraction orders as a function of θ_{QWP}. The different lines correspond to different diffraction orders, and they are color-coded as described in Fig. 5a. Since all k-space patterns are symmetric along y, here we focus only on diffraction orders with $m_y \geq 0$. To aid comparison, all experimental curves in Fig. 5(b-e) have been normalized to the highest global intensity. Figure 5b shows the intensity of four diffraction orders with $(m_x \geq 0, m_y \geq 0)$. The intensity of all these diffraction orders features a strong dependence on the pump ellipticity, and the intensity of each order can be reduced to almost zero for selected values of θ_{QWP}. In Fig. 5(c-e) we compare the intensities of three pairs of diffraction orders $(\pm m_x, m_y)$, corresponding to specular emission directions with respect to the x-axis. Figure 5c-e confirm that, apart from small deviations due to experimental imperfections mentioned above, the intensity curve of each diffraction order (m_x, m_y) matches the one of the corresponding opposite order $(-m_x, m_y)$ when the mirror transformation $\theta_{QWP} \rightarrow 90° - \theta_{QWP}$ is applied. Moreover, for all pairs of diffraction orders it is possible to find values of θ_{QWP} for which one diffraction order completely dominates over its specular partner. This strong pump-polarization-induced directionality is particularly evident for the diffraction orders $(\pm 3, 1)$, shown in Fig. 5e, which were indeed the targeted diffraction orders of the designed metasurface. The intensity of the $(-3,1)$ diffraction order (dashed green line) peaks at $\theta_{QWP} = 50°$ (corresponding to an almost L-polarized pump), while it remains very low for $\theta_{QWP} > 100°$. On the contrary, the intensity of the $(+3,1)$ diffraction order (solid green line) peaks at $\theta_{QWP} = 125°$ (almost R-polarized pump), while it remains very low for $\theta_{QWP} < 90°$. The measured extinction ratios of the diffraction order intensities is $I_{(-3,1)}/I_{(3,1)} \approx 155$ at $\theta_{QWP} = 50°$ and $I_{(3,1)}/I_{(-3,1)} \approx 164$ at $\theta_{QWP} = 125°$.

3 Discussions

In this work, we demonstrated diffractive nonlinear nonlocal metasurfaces for simultaneous efficiency enhancement through lattice resonances and subwavelength spatial control over the wavefront of third-harmonic generation. We designed a-Si metasurfaces supporting a highly delocalized resonance at approximately 1530 nm and a Q-factor of ~180. To showcase the capabilities of our approach to manipulate the wavefront of the emitted light at the TH, we developed a steering metasurface which, based on a Pancharatnam-Berry phase, generates structured light with resonant light-matter enhancement. From the measurements, we estimate a peak efficiency of $\eta \approx 8.5 \cdot 10^{-13} W^{-2}$, which is almost two orders of magnitudes larger than previously reported nonlinear gradient metasurfaces [32, 34]. While in the device demonstrated here the THG efficiency is only

boosted within a narrow spectral range, our approach does not inherently rely on utilizing a narrow resonant mode, and it can be readily extended to different structures supporting broader resonances and/or stronger nonlinearities. In contrast to previous efforts on nonlinear Pancharatnam-Berry phase, in which the generated harmonic light is circularly polarized, here we demonstrate a nonlinear process imparting a geometric phase onto a linearly polarized harmonic component, associated with the qBIC features. This feature demonstrates a novel mechanism for nonlinear metasurfaces, which exploits both the advantages of nonlocal metasurfaces and local patterning of the generated wavefront, enhancing the efficiency of nonlinear processes while providing subwavelength control over the properties of the generated light. These results extend the applicability of spatially varying nonlocal metasurfaces to nonlinear optics, enabling a powerful extension of the physics of nonlinear geometric phase beyond circular polarization. This platform establishes a new pathway towards the development of nonlinear nanoscale devices with complete nanoscale control over the optical properties of the generated light, applicable in both classical and quantum domains, without the requirement of phase matching. Moreover, our approach is agnostic to the specific material as it relies only on geometrical features, and the same concepts and designs could be applied to metasurfaces made of materials different than silicon such as GaAs [17, 42, 43], and intersubband transitions in multi-quantum-well semiconductor heterostructures [44] where different symmetries of the second or third-order nonlinear permittivity tensor will result in different phase and polarization features.

4 Methods

4.1 Numerical calculations

Fully vectorial numerical calculations are performed in the frequency-domain with the finite element method implemented in COMSOL. The eigenmodes of the structure are calculated with the eigenmode solver. Open boundaries conditions are implemented with perfectly matched layers, while periodic boundaries with Floquet conditions are used for planes perpendicular to the metasurface. The transmittance spectra are obtained using periodic ports. The dispersion of the materials is introduced in the numerical calculations. The third harmonic signal is calculated using a two-step procedure. First the electric field at the pump frequency is numerically calculated. Second, the optical response of the metasurface at the third-harmonic frequency is calculated by setting a nonlinear polarization generated by the electric field distribution at the pump frequency.

4.2 Fabrication

The samples were fabricated with a standard top-down lithographic approach, starting with commercially available quartz substrates. The substrates were cleaned via an acetone bath inside an ultrasonic cleaner, followed by an oxygen-based cleaning plasma (PVA Tepla IoN 40). After cleaning, amorphous silicon (α-Si) was deposited on the substrates via a plasma-enhanced chemical vapor deposition (PECVD) process. A layer of E-beam resist (ZEP 520-A) was then spin-coated on top of the samples. To avoid any charging effect during electron-beam lithography, a thin layer of an anti-charging polymer (DisCharge, DisChem) was additionally spun on the sample. The desired pattern was then written with an electron beam tool (Elionix 50 keV). The anti-charging layer was removed with water, and the exposed ZEP was developed with n-amyl acetate followed by a rinse in isopropanol. The pattern was then transferred to the underlying silicon layer via dry etching in an ICP machine (Oxford PlasmaPro System 100). The resist mask was finally removed with a solvent (Remover PG).

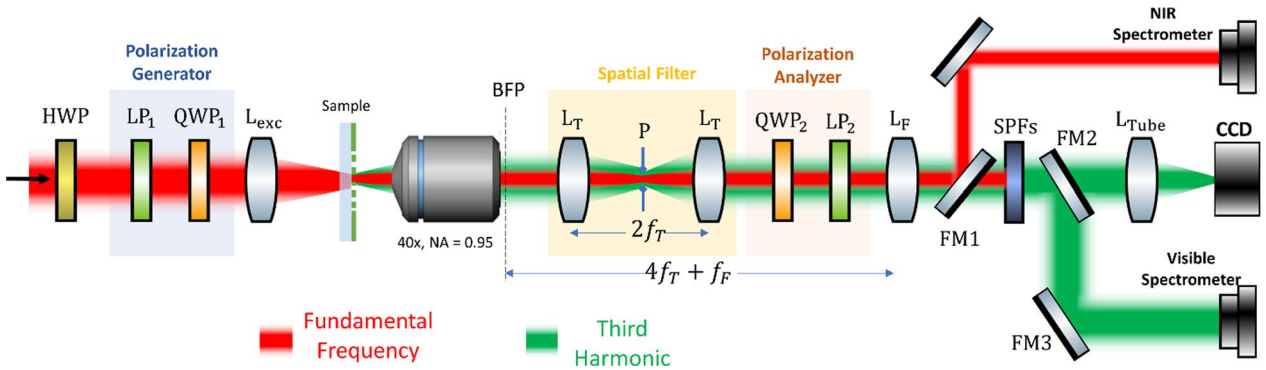

Fig. 6 Setup used to measure polarization-dependent k-space emission patterns. See text for details

4.3 Experimental setups

All data in Figs. 3–5 (except for the transmission spectrum in Fig. 3b) were acquired with the setup shown in Fig. 6 (see also ref. [45]) The pump signal at the FF was created by an optical parametric oscillator (APE, Levante IR ps), which generates a tunable pulsed laser (pulse duration $\tau = 2$ ps, repetition rate $f = 80$ MHz). The power and polarization of the pump laser were controlled by a half-wave plate (HWP), a linear polarizer (LP_1) and a quarter-wave plate (QWP_1) cascaded in sequence. The laser was then focused on the sample (from the quartz side) with a long-focal-length lens (L_{exc}, focal length = 20 cm). The excitation spot had a diameter of approximately 140μm. In all measurements, the pump was always impinging on the sample at normal incidence. The signal propagating on the other side of the sample (containing both the pump and the TH emission) was collected by a high-NA objective (Nikon, 40x, NA = 0.95). A 1:1 telescope (formed by two lenses with focal length $f_T = 5$ cm) and a 400-μm-diameter pinhole were used as a spatial filter to ensure that only the signal coming from a circular area of diameter ≈ 75 μm on the sample was collected. After the telescope, the desired polarization of the TH signal was extracted with a polarization analyzer formed by a quarter-wave plate (QWP_2) and a linear polarizer (LP_2). A Fourier lens (L_F, focal length $f_F = 20$ cm) was mounted on a flip stage, allowing either the real space or the back focal plane of the objective to be imaged. Finally, a tube lens (L_{Tube}) focused the light on a silicon CCD camera. The pump signal was filtered out with the aid of two short-pass filters (SPFs). Two mirrors, placed on flip stages (FM1 and FM2), allowed redirecting the output signal either to a NIR spectrometer (for spectral characterization of the pump) or to a visible spectrometer (for spectral characterization of the TH signal).

The efficiency measurements shown in Figs. 3(b-c) were performed with a modified version of the setup shown in Fig. 6. A beam sampler and a reference photodiode (connected to a lock-in amplifier) were added in the excitation path, in order to accurately monitor the pump power level in real time. The pump polarization was fixed to horizontal. In the collection path, the objective was replaced by a lens (focal length 5 cm, NA = 0.25). The spatial filter and the Fourier lens were removed, and the polarization analyzer was set to horizontal. After passing through the SPFs filters, the THG signal was measured with a Si photodiode (Thorlabs, DET100A2), connected to another lock-in amplifier. Both photodiodes were calibrated with the aid of thermal powermeters. For the calibration of the silicon photodiode, a strong TH signal was generated by sending the pump laser into a commercially available frequency converter (APE, HarmoniXX SHG/THG). Then, for any given pump wavelength, the pump power was varied continuously by rotating the HWP, and the signal measured by the two photodiodes was acquired.

The transmission spectrum (blue line in Fig. 3b) was measured with a different setup (described also in ref. 25), where the excitation was provided by a broadband light and the signal was collected by a low-NA lens and sent directly to the NIR spectrometer.

Supplementary Information

The online version contains supplementary material available at https://doi.org/10.1186/s43593-025-00116-7.

Supplementary material 1

Acknowledgements

This work was supported by the Department of Defense and the Simons Foundation. L. C. was supported by the European Union's Next Generation EU Mission 4 Component 1, PRIN 2022– NoLimiTHz (2022BC5BW5).

Author contributions

L.C., A.O. and A.A. developed the theoretical model. L.C. performed the numerical simulations. M.C. fabricated the samples, performed the experimental measurements and analyzed the data with the assistance of L.C. and A.O. A.A. supervised the project. All authors contributed to the paper writing.

Data availability

The data presented in the paper are available upon request.

Declarations

Competing interests

The authors have no conflict of interest.

Received: 20 March 2025 Revised: 31 October 2025 Accepted: 5 November 2025
Published online: 02 February 2026

References

1. N. Yu et al., Light propagation with phase discontinuities: generalized laws of reflection and refraction. Science **334**, 333–337 (2011)
2. N. Yu, F. Capasso, Flat optics with designer metasurfaces. Nat. Mater. **13**, 139–150 (2014)
3. S.C. Malek, A.C. Overvig, A. Alù, N. Yu, Multifunctional resonant wavefront-shaping meta-optics based on multilayer and multi-perturbation nonlocal metasurfaces. Light Sci. Appl. **11**, 246 (2022)
4. Y. Zhou, H. Zheng, I.I. Kravchenko, J. Valentine, Flat optics for image differentiation. Nat. Photonics **14**, 316–323 (2020)
5. M. Cotrufo, A. Arora, S. Singh, A. Alù, Dispersion engineered metasurfaces for broadband, high-NA, high-efficiency, dual-polarization analog image processing. Nat. Commun. **14**, 7078 (2023)
6. F. Zangeneh-Nejad, D.L. Sounas, A. Alù, R. Fleury, Analogue computing with metamaterials. Nat. Rev. Mater. **6**, 207–225 (2021)
7. E. Tseng et al., Neural nano-optics for high-quality thin lens imaging. Nat. Commun. **12**, 6493 (2021)
8. L. Huang, S. Zhang, T. Zentgraf, Metasurface holography: from fundamentals to applications. Nanophotonics **7**, 1169–1190 (2018)
9. H. Ren et al., Metasurface orbital angular momentum holography. Nat. Commun. **10**, 2986 (2019)
10. J. Li et al., Addressable metasurfaces for dynamic holography and optical information encryption. Sci. Adv. **4**, eaar6768 (2018)

11. S. Kruk, Y. Kivshar, Functional meta-optics and nanophotonics governed by Mie resonances. ACS Photon. **4**, 2638–2649 (2017)
12. S.M. Kamali, E. Arbabi, A. Arbabi, A. Faraon, A review of dielectric optical metasurfaces for wavefront control. Nanophotonics **7**, 1041–1068 (2018)
13. S. Chang, X. Guo, X. Ni, Optical metasurfaces: progress and applications. Annu. Rev. Mater. Res. **48**, 279–302 (2018)
14. P. Genevet, F. Capasso, Holographic optical metasurfaces: a review of current progress. Rep. Prog. Phys. **78**, 024401 (2015)
15. S. Zhang, H. Zhou, B. Liu, Z. Su, L. Huang, Recent advances and prospects of optical metasurfaces. ACS Photonics (2023). https://doi.org/10.1021/acsphotonics.2c01539
16. Y. Yang et al., Nonlinear fano-resonant dielectric metasurfaces. Nano Lett. **15**, 7388–7393 (2015)
17. S. Liu et al., Resonantly enhanced second-harmonic generation using III–V semiconductor all-dielectric metasurfaces. Nano Lett. **16**, 5426–5432 (2016)
18. Z. Liu et al., High-Q quasibound states in the continuum for nonlinear metasurfaces. Phys. Rev. Lett. **123**, 253901 (2019)
19. L. Carletti et al., Steering and encoding the polarization of the second harmonic in the visible with a monolithic LiNbO3 metasurface. ACS Photonics **8**, 731–737 (2021)
20. T. Santiago-Cruz et al., Photon pairs from resonant metasurfaces. Nano Lett. **21**, 4423–4429 (2021)
21. J. Zhang et al., Spatially entangled photon pairs from lithium niobate nonlocal metasurfaces. Sci. Adv. **8**, eabq4240 (2022)
22. S.A. Mann et al., Ultrafast optical switching and power limiting in intersubband polaritonic metasurfaces. Optica **8**, 606–613 (2021)
23. M. Cotrufo et al., Intersubband polaritonic metasurfaces for high-contrast ultra-fast power limiting and optical switching. NPJ Nanophotonics **1**, 14 (2024)
24. C. McDonnell, J. Deng, S. Sideris, T. Ellenbogen, G. Li, Functional THz emitters based on Pancharatnam-Berry phase nonlinear metasurfaces. Nat. Commun. **12**, 30 (2021)
25. M. Cotrufo, A. Cordaro, D.L. Sounas, A. Polman, A. Alù, Passive bias-free non-reciprocal metasurfaces based on thermally nonlinear quasi-bound states in the continuum. Nat. Photonics (2023). https://doi.org/10.1038/s41566-023-01333-7
26. King, J. *et al.* Electrically tunable VO2-metal metasurface for mid-infrared switching, limiting, and nonlinear isolation. *arXiv preprint* arXiv:2303.09060 *(2023).*
27. L. Carletti et al., Nonlinear THz generation through optical rectification enhanced by phonon-polaritons in lithium niobate thin films. ACS Photonics **10**, 3419–3425 (2023)
28. C. Gigli et al., Tensorial phase control in nonlinear meta-optics. Optica **8**, 269–276 (2021)
29. L. Wang et al., Nonlinear wavefront control with all-dielectric metasurfaces. Nano Lett. **18**, 3978–3984 (2018)
30. M. Tymchenko et al., Gradient nonlinear pancharatnam-berry metasurfaces. Phys. Rev. Lett. **115**, 207403 (2015)
31. B. Liu et al., Nonlinear wavefront control by geometric-phase dielectric metasurfaces: influence of mode field and rotational symmetry. Adv. Opt. Mater. **8**, 1902050 (2020)
32. B. Reineke Matsudo et al., Efficient frequency conversion with geometric phase control in optical metasurfaces. Adv. Sci. **9**, 2104508 (2022)
33. A. Karnieli, Y. Li, A. Arie, The geometric phase in nonlinear frequency conversion. Front. Phys. **17**, 12301 (2022)
34. B. Liu et al., Nonlinear dielectric geometric-phase metasurface with simultaneous structure and lattice symmetry design. ACS Photonics **10**, 4357–4366 (2023)
35. A. Overvig, A. Alù, Diffractive nonlocal metasurfaces. Laser Photon. Rev. **16**, 2100633 (2022)
36. A.C. Overvig, S.C. Malek, N. Yu, Multifunctional nonlocal metasurfaces. Phys. Rev. Lett. **125**, 017402 (2020)
37. M. Cotrufo, A. Alù, Metamaterials for analog all-optical computation. Prog. Opt. **69**, 211 (2024)
38. K. Koshelev, A. Bogdanov, Y. Kivshar, Meta-optics and bound states in the continuum. Sci. Bull. **64**, 836–842 (2019)
39. V. Zubyuk, L. Carletti, M. Shcherbakov, S. Kruk, Resonant dielectric metasurfaces in strong optical fields. APL Mater. (2021). https://doi.org/10.1063/5.0048937
40. S.C. Malek, A.C. Overvig, S. Shrestha, N. Yu, Active nonlocal metasurfaces. Nanophotonics **10**, 655–665 (2020)
41. Y. Meng et al., Optical meta-waveguides for integrated photonics and beyond. Light Sci. Appl. **10**, 235 (2021)
42. L. Carletti, D. Rocco, M.A. Vincenti, D. de Ceglia, C. De Angelis, Intrinsic nonlinear geometric phase in SHG from zincblende crystal symmetry media. Nanophotonics **13**, 3321–3326 (2024)
43. M. Cotrufo et al., Nonlinear analog processing with anisotropic nonlinear films. Nanophotonics (2025). https://doi.org/10.1515/nanoph-2024-0770/html
44. J. Lee et al., Giant nonlinear response from plasmonic metasurfaces coupled to intersubband transitions. Nature **511**, 65–69 (2014)
45. M. Cotrufo, C.I. Osorio, A.F. Koenderink, Spin-dependent emission from arrays of planar chiral nanoantennas due to lattice and localized plasmon resonances. ACS Nano **10**, 3389–3397 (2016)